



Transition metal enhanced chromium nitride as composite nitrogen carrier for sustainable chemical looping ammonia synthesis

Sijun Wang^{a,1}, Feng Gong^{a,*,1}, Qiang Zhou^b, Yunlong Xie^c, Hao Li^d, Menglin Li^a, Enkang Fu^a, Peng Yang^a, Yuhang Jing^a, Rui Xiao^a

^a Key Laboratory of Energy Thermal Conversion and Control of Ministry of Education, School of Energy and Environment, Southeast University, Nanjing 210096, China

^b Department of Engineering, The University of Tokyo, Tokyo, Japan

^c Institute for Advanced Materials, Hubei Normal University, Huangshi 435002, China

^d Department of Mechanical Engineering, The University of Hong Kong, Hong Kong Special Administrative Region of China

ARTICLE INFO

Keywords:

Chemical looping
Ammonia synthesis
Composite nitrogen carrier
Ammonia selectivity
Lattice nitrogen transfer

ABSTRACT

Chemical looping ammonia synthesis (CLAS) is promising to achieve decentralized ammonia synthesis under ambient pressure. Here, we develop a highly selective composite nitrogen carrier for efficient CLAS based on transition metals (TMs=Co, Ni, Fe) decorated chromium nitride (CrN). Systematic studies indicate that the pristine CrN is extremely inert: only 4.5% lattice nitrogen can be consumed in reacting with H₂ (700 °C, 1 bar). Upon loading cobalt, the composite nitrogen carrier achieves lattice nitrogen conversion of 50.7% and ammonia selectivity up to 98.1%. Furthermore, Co-CrN exhibits excellent CLAS performance, attaining an average ammonia production rate of 466.1 μmol g⁻¹ h⁻¹ in 12 chemical loopings, which is ~10 times that of the pristine CrN. Theoretical calculations reveal that the nitrogen vacancies generated in hydrogenation play a crucial role as activation centers for N₂ fixation through a Mars–van Krevelen mechanism. This work provides a novel strategy to optimize nitrogen carriers for enhanced CLAS.

1. Introduction

As an essential nitrogen fertilizer and raw chemical ingredient, ammonia has changed the trajectory of human society [1,2]. With the development of hydrogen energy, ammonia has been investigated as a promising renewable hydrogen carrier because of its high energy density (3 kWh/kg) and ease of storage and transportation [3]. However, the current industrial ammonia synthesis is still dominated by the Haber-Bosch (H-B) process which is operated under harsh conditions (350–550 °C, 10–30 MPa). The high-pressure in the H-B process is essential and comprises more than 50% of the total capital expenditures, which inevitably hinders its decentralized ammonia production [4–6]. Thus, there is a high demand to develop alternative approaches for sustainable ammonia synthesis under mild conditions [7,8].

Chemical looping ammonia synthesis (CLAS) is a promising route to avoid the strict operating requirement in the H-B process for decentralized ammonia synthesis. It employs nitrogen carriers to separate the overall ammonia synthesis into two reaction steps: nitridation and ammoniation, which allows each step to occur under optimal conditions

[9,10]. Thus, CLAS can independently optimize the kinetic and thermodynamic parameters of these steps and achieve ammonia production at atmospheric pressure. This feature further liberates the ammonia synthesis process in time and space (such as remote energy utilization), thereby giving feasibility for designing localized and miniaturized ammonia production facilities [11–13].

Numerous studies have been conducted to develop stable and efficient nitrogen carriers for CLAS. Among them, transition metal nitrides (TMNx) with active lattice nitrogen have been explored for more than a century [14,15]. A variety of binary nitrides, such as Ca₃N₂ [13], Ni₃N [16], Ta₃N₅ [16,17], Re₃N [18], Mo₂N [19], Mn₃N₂ [20], iron nitride [21,22], were confirmed to react with H₂ and release NH₃, because of their capability of nitrogen transfer [23]. Moreover, Hargreaves et al. reported that the lattice nitrogen in Mo-based nitrides could be regenerated by activating N₂ [24,25]. They subsequently identified the homomolecular and heterolytic nitrogen exchange of CoMoNx via an isotope method, further demonstrating the exchangeability of the surface nitrogen species [26,27]. Density Functional Theory (DFT) calculations revealed that nitrogen vacancies (generated by hydrogenation)

* Corresponding author.

E-mail address: gongfeng@seu.edu.cn (F. Gong).

¹ S. Wang and F. Gong contributed equally to this work.

tend to bind N_2 strongly and reduce the energy barrier to break the strong $N\equiv N$ bond [28]. The formation and recovery of nitrogen vacancies are consistent with the famous Mars–van Krevelen mechanism [29,30]. Accordingly, transition metal nitrides are believed to function as a storage medium for the activated nitrogen, thus a prospective nitrogen carrier for CLAS.

Although CLAS can circumvent the competition adsorption of reacting species, TMNx confronts a dilemma of reactivity and selectivity, referred to as another “scaling relationship” [9,31]. This “scaling relationship” is illustrated by the fact that the energy barriers of lattice nitrogen hydrogenation and N_2 activation (for nitridation) in TMNx scale with each other [11,13]. Furthermore, as the formation energy of nitrogen vacancy (V_N) increases, higher temperatures are required for the hydrogenation to produce ammonia due to the strong bonding between the metal and lattice nitrogen. Conversely, TMNx with lower formation energy is more unstable, while it is easier to transfer the lattice nitrogen out, and the transferred lattice nitrogen is more inclined to deplete as N_2 [28]. In the meantime, the regeneration of these TMNx is also difficult to achieve under mild conditions. Consequently, TMNx exhibits an antagonistic relationship between lattice nitrogen conversion and ammonia production selectivity. To obtain higher ammonia production, some attempts of composite nitrogen carriers have achieved remarkable improvement in boosting their lattice nitrogen conversion [7,32–38]. For instance, cobalt was reported to be able to activate tantalum nitride, and the ammonia production was boosted by around 6.8 times [17]. Metal-enhanced Mn_3N_2 was employed in CLAS as a further typical work, and the ratio of lattice nitrogen converted to NH_3 was increased from 3.1% to 15.1% with the decoration of Li [20]. However, the improved nitrogen reactivity of TMNx above was still accompanied with low NH_3 selectivity, forming again the limitation of CLAS. In the study of A- Mn_3N_2 (A=Fe, Co, K, and Li), the addition of dopants could accelerate lattice nitrogen depletion as N_2 , losing over 84% of the reacted nitrogen [20]. Besides, doping Li metals may also hinder the regeneration process on the surface of reduced nitrides. $Ta_{3-x}Co_xN_y$ exhibited a higher conversion selectivity attributed to the stronger combination of Ta and N, which varies significantly relating the content of Co [17]. In summary, designing a synergistic composite nitrogen carrier requires a strategy that simultaneously focuses on NH_3 selectivity while activating lattice nitrogen.

In this work, we focus on the controlled conversion of lattice nitrogen in TMNx and propose a novel avenue for designing highly selective composite nitrogen carriers. Based on the thermodynamic property of TMNx, we identified a nitride with strong metal-nitrogen bonding but high NH_3 selectivity (chromium nitride, CrN) [13]. Subsequently, CrN was decorated with various transition metals for a boosted reactivity in producing NH_3 . Experimental results manifested the activation of lattice nitrogen in TM-CrN, and encouragingly, they maintained a high selectivity in reacting with H_2 . The cyclic performance of TM-CrN was further evaluated. Finally, theoretical calculations were performed to investigate the path of atom transfer and the variation of the rate-determining step in a chemical looping cycle. The modulation of chromium nitride may facilitate the innovation of composite nitrogen carriers and promote the application of ammonia in structuring “hydrogen energy” systems.

2. Experimental

2.1. Materials preparation

2.1.1. Synthesis of Cr-urea precursor

Chromium-urea coordination compound as a precursor was synthesized via a reaction of chromium chloride and urea. Typically, a concentrated solution was obtained by dissolving 0.04 mol $CrCl_3 \cdot 6H_2O$ (Sigma-Aldrich, 98.0%) in 15 ml anhydrous ethanol. The solution was added dropwise to a saturated urea/ethanol solution (0.24 mol urea (Macklin, 99.5%) dissolved in 20 ml ethanol) with stirring at 80 °C until

green precipitates formed [39]. Bulk Cr-urea precursor was separated from the solution by filtering and the obtained precursor was kept overnight at 80 °C in a vacuum oven.

2.1.2. Synthesis of CrN

In a typical synthesis, 4.2 g ground Cr-urea precursor was loaded in a quartz boat and placed in a tube furnace for ammonia pyrolysis. Before heating, a gas mixture of NH_3 (50%) + N_2 (50%) was allowed to pass through for 1 h to remove the air from it. The precursor was heated at a rate of 5 °C min^{-1} under the same gas mixture (80 ml min^{-1}) up to 750 °C, kept for 6 h, and cooled to room temperature [40]. The dark-gray product was collected, pulverized, and sealed for storage.

2.1.3. Synthesis of TM-CrN

Metal-doped chromium nitride was prepared using an isovolumic impregnation method [41,42]. In a case of doping 10 wt% cobalt, 0.2933 g $Co(NO_3)_2 \cdot 6H_2O$ (Macklin, 99.0%) was dissolved in 4 ml ethanol and stirred until a homogeneous solution formed. Then 4.2 g Cr-urea precursor was added into the above solution, agitated at room temperature with a glass rod, and ultimately dried in a vacuum oven for 8 h. The impregnated precursor material was then ground to a fine powder for the same ammonia pyrolysis treatment as described in the synthesis of CrN. Similar procedure was conducted to dope other transition metals, using a corresponding mass of metal nitrates as the metal source (Fig. 1). Ethanol is a desirable impregnating solvent since the precursor is insoluble in ethanol but extremely soluble in water [43]. Additionally, the low surface tension of ethanol makes it easier to enter the interstitial space of precursor, and the volatility of ethanol creates a concentration gradient that facilitates the diffusion of the active component [44,45].

2.2. Materials characterization

X-ray diffraction (XRD) pattern of the samples was measured on a Rigaku Ultima IV diffractometer with Cu K α radiation ($\lambda = 0.15418$ nm) operated at 40 kV and 40 mA. The scanning range (2-theta) was performed between 10°–80° with a step size of 0.02°. The X-ray photoelectron spectroscopy (XPS) measurement was carried out on an ESCALAB 250Xi spectrometer (Thermo Scientific, USA) equipped with a pass energy of 30 eV, a power of 100 W (10 kV and 10 mA), and a monochromatized Al-K α X-ray ($h\nu = 1486.65$ eV) source. All samples were analyzed under a pressure of less than 1.0×10^{-9} Pa. Spectra were acquired through the advantage software (Version 5.979) with a step of 0.05 eV. Scanning electron microscopy (SEM) and corresponding element dispersion images were obtained using a Hitachi Regulus 8100. Transmission electron microscopy (TEM) and High-resolution TEM were



Fig. 1. Preparation of Cr-based nitrogen carriers via impregnation and ammonolysis methods.

further performed to characterize the morphologies and microstructures using a Tecnai F20.

H₂-temperature programmed reduction (H₂-TPR) was conducted on a PCA-1200 chemical adsorption analyzer. Prior to measurements, a batch of the sample (50 mg) was heated (10 °C min⁻¹) to 200 °C under a continuous flow of Ar (30 ml min⁻¹) for a drying pretreatment. The temperature was maintained for 30 min to remove any possible impurities, such as H₂O or weakly adsorbed NH₃. After cooling to the ambient temperature, the gas was switched to 20% H₂/Ar (30 ml min⁻¹) and the temperature was controlled to 800 °C at a ramping rate of 10 °C min⁻¹. The exhaust gases were analyzed by a thermal conductivity detector (TCD). N₂-Thermogravimetric Analysis (N₂-TG) was conducted on a Discovery TGA 5500 analyzer to investigate the N₂ fixation performance of the reduced nitrogen carriers. All samples were pretreated in a tube furnace with a flow of 5% H₂/Ar, which was kept at 700 °C for 4 h. In both cases, 10 mg samples were heated to 700 °C in a crucible at a rate of 5 °C min⁻¹. Purified N₂ (60 ml min⁻¹) was used as the carrier gas. Elemental analysis was performed by combustion using an Elemental Unicube analyzer in CHNS model. Accuracy was ensured by repeating the measurement at least three times.

2.3. Catalytic performance evaluation

Schematic diagram of the evaluation system for CLAS experiment is shown in Fig. S1. H₂ and N₂ (60 ml min⁻¹) was passed alternatively in a fixed-bed reactor containing 60 mg of the as-prepared nitrogen carriers, and the tail gas was introduced to a tank containing diluted H₂SO₄ solution (1.0 mmol·l⁻¹, 200 ml at 25 °C). The released NH₃ via hydrogenation reacts easily with H⁺ (NH₃ + H⁺ → NH₄⁺), and then the formation of NH₄⁺ creates a linear proportion between the decrease in conductivity (Δκ) and the amount of ammonia production (Δn_{NH₃}) [7,46]. The principle of NH₃ production detection and the related computational methods are described in Supplementary Method 1. Furthermore, the indophenol blue method was employed for additional ammonia quantification (Supplementary Method 2), showing a variation of less than 5% with the conductivity method. This verifies the reliability of the conductivity method for ammonia detection (Table S1).

The rate of ammonia production for CLAS was calculated based on:

$$r_a = \frac{\Delta n_{(\text{NH}_3)}}{m(t_{\text{H}_2} + t_{\text{N}_2})} \quad (\text{R1})$$

where r_a is the average NH₃ production rate in a single loop (μmol g⁻¹ h⁻¹), Δn_{NH₃} is the produced ammonia (μmol), m is the mass of the Cr-based nitrogen carriers (g), t_{H_2} and t_{N_2} are the time of hydrogenation and nitridation (h), which are respectively optimized to achieve the highest ammonia production rate.

2.4. Computational calculations

Density Functional Theory (DFT) calculations involved in this study were conducted using the Vienna Ab Initio Simulation Package (VASP) [47]. The generalized gradient approximation (GGA) with the Perdew-Burke-Ernzerhof (PBE) functional was adopted to describe the exchange-correlation effect, and the projector augmented wave (PAW) method was employed to describe the core electrons [48,49]. DFT-D3 method was employed to depict the long-range vdW interactions in a weak binding system [50–52]. Spin polarization was considered in all calculations, and the initial magnetic moments of the Cr were set to 3, –3, etc. for the anti-magnetism of CrN. A cutoff energy of 400 eV and a Monkhorst-Pack K-mesh of 3 × 3 × 1 were selected to sample the Brillouin zone unless otherwise specified [53]. To achieve a fully relaxed geometry, 10⁻⁵ eV was used as the energy convergence threshold, and 0.02 eV/Å was used as the criterion for force convergence on each atom. The CrN(001) substrate was modeled by a 4-layer slab with a 4 × 4 lateral unit cell. A vacuum layer of 20 Å was established to eliminate the

interaction between adjacent layers. And a model of the Co₈ cluster was derived from bulk metal and preoptimized for theoretical insight into the activation effect of Co (Supplementary Method 3).

The transition states were calculated as the minimum energy path in a primitive reaction with the climbing image-nudged elastic band (CI-NEB) method. Eight images were inserted between the initial and final states for precise atomic migration investigation [54,55]. The computational equation of adsorption energy, N-vacancy formation energy (E_{NV}), and energy barriers, etc. are presented in Supplementary Method 4 [56,57].

3. Results and discussion

3.1. Characterization of chromium nitride

Cr-based nitrogen carriers with high performance and stability were synthesized by pyrolyzing the Cr-Urea precursor in an ammonia-containing stream (Fig. 1). TM clusters were uniformly loaded via an isovolumic impregnation method with ethanol as the solvent. The formation of CrN follows a nucleation and growth mechanism [39], which crystallizes in the cubic rock salt structure. Fig. 2a shows the XRD patterns of the pristine CrN and TM-CrN. The significant diffraction peaks at 37.6°, 43.7°, 63.5°, and 76.2° correspond to the (111), (200), (220), and (311) facets of CrN (PDF #76-2494), respectively, indicating a high crystallinity of the as-prepared nitrides. Furthermore, faint peaks of Co and Ni were observed in the XRD patterns of Co- or Ni-loaded CrN, and Fe₃N peaks were identified in Fe-CrN. The presence of these peaks demonstrates the successful loading of transition metals in TM-CrN. No peaks of impurities such as metal oxides or residual carbon were detected. The XRD pattern of the Cr-urea precursor is shown in Fig. S3, indicating the formation of a metal-urea complex through bonding [39, 58].

In all TM-CrN, Co-CrN with the highest NH₃ production amount was chosen for subsequent investigation. X-ray photoelectron spectroscopy (XPS) was conducted to analyze the surface chemical state of the selected nitrogen carrier. The XPS survey spectrum in Fig. 2b manifests the presence of Cr, Co, N, O, etc., and C and Cl were derived from the Cr-urea precursor residue. Fig. 2c displays the Cr 2p spectra with peaks at 574.6 eV (2p_{3/2}), 575.6 eV (2p_{3/2}), and 576.7 eV (2p_{3/2}), which correspond to the mono Cr, unoxidized CrN, and Cr₂O₃, respectively [59,60]. Spontaneous oxidation has been reported to occur on the surface of CrN, where the surface oxygen content was measured at 20.60 at% increasing from 5.66 at% (atomic percentage) [43]. In this work, the observed oxide surface layer (<1 nm, as the Cr₂O₃ phase was identified in XPS but undetected in XRD) is suggested to inhibit internal oxidation, thus explaining the durability of the Cr-based nitrogen carriers even stored in an oxygen-containing state [61]. Furthermore, the major peaks at 780.9 eV (2p_{3/2}) and 796.9 eV (2p_{1/2}) in the spectrum of Co 2p can be ascribed to the peaks of Co²⁺ in CoO and Co³⁺ in Co₂O₃, respectively (Fig. S4a) [62]. The preceding discussion on the valence state of Co simultaneously verifies the surface oxidation property of Co-CrN. It is notable that the spectrum of N 1s contains only two peaks, where the peak at 396.8 eV represents the lattice-N in CrN (17.35 at%) and the other peak at 398.9 eV is possibly ascribed to the amino- (NH₂-) or ammonia (NH₃) N (4.58 at%) (Fig. S4) [43]. Hence, the atomic ratio of lattice-N to Cr is estimated to be 0.98:1, where the atomic concentration of Cr on the surface is estimated to be 17.66 at%. This indicates that the nitrogen is highly selectively transferred without the formation of Cr-N_xO_y [63]. Fig. S5 shows the spectra of impurity elements including C and O. In the analysis of the O 1s spectrum, the peaks at 529.95 eV and 531.45 eV correspond to metal oxides, while the peak at 533.95 eV may be attributed to the deliquescence of residual chlorides. These results provide a chemical insight into the modulation of nitrogen carriers with transition metals.

The obtained Co-CrN exhibits a near-spherical morphology as shown in Fig. 2d. Comparisons of the SEM images of TM-CrN revealed similar

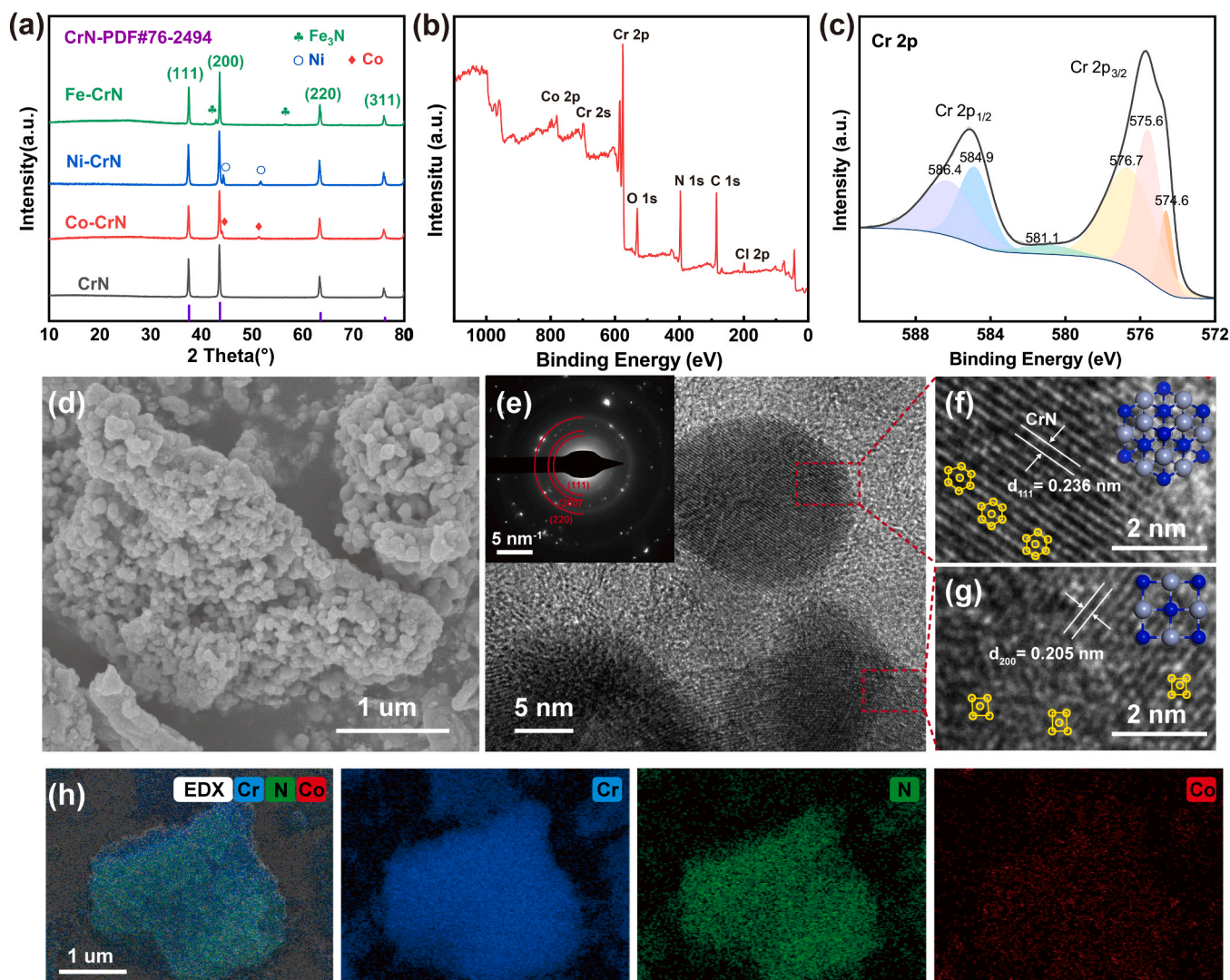


Fig. 2. Characterization of Cr-based nitrogen carriers. (a) XRD patterns of the pristine CrN and TM-CrN (TM=Co, Ni, Fe). High-resolution XPS spectra of Co-CrN: (b) survey spectrum, and (c) Cr 2p. (d) SEM images of Co-CrN. (e) High-resolution TEM image of Co-CrN with the corresponding selected area electron diffraction (SAED) pattern. (f, g) High-resolution TEM images of selected regions of the particles shown in (e). (h) SEM-EDX mapping images of Co-CrN with the homogeneous elemental distribution.

nanoparticles (Fig. S6), where obvious surface intergrowth was observed with the loading of Fe. Further investigation indicated that CrN loaded with various transition metals exhibited significantly different particle sizes (Fig. S7). Co-CrN showed the smallest particle size (62 ± 11 nm in diameter), which plays a significant role in determining the specific surface area and the exposure of active sites. Fig. S8 presents the influence of Co amount and it is revealed that the higher loading amount (15 wt%), contrary to the moderate level (10 wt%), caused an increase in particle size. SEM-EDX mapping of Cr-based nitrogen carriers manifests the chemical homogeneity of Co-CrN (Fig. 2h and Fig. S9). The statistics of surface element analysis indicates that the actual loading amount of TMs is generally lower than the calculated, as shown in Table S2. Fig. 2e shows the HR-TEM image and the corresponding selected area electron diffraction (SAED) pattern of Co-CrN. The bright rings in the inner circle match well with the (111), (200), and (220) facets of CrN identified by the XRD pattern. Atom-resolved HR-TEM images display clear lattice fringes with spacing of 0.236 and 0.205 nm along the direction of (111) and (200), also in line with the ref. value of CrN (Fig. 2f, g and Fig. S10). The inserted marks denote the crystal structure of CrN in the corresponding direction. Moreover, no lattice of any surface oxide was observed in HR-TEM, which suggests that the thin

oxidized layer is capable to protect inner atoms from further oxidation [61,64].

3.2. Nitrogen transfer properties of Cr-based nitrogen carriers

Cr-based nitrogen carriers are capable to convert the lattice nitrogen into NH_3 , acting as a nitrogen transfer reagent. To reveal the influence of TM decoration on the hydrogenation reactivity, a batch of as-prepared nitrides were subjected to the H_2 -TPR test (Fig. 3a). With the increase of temperature, the reduction peak of the pristine CrN was observed until 718°C . Upon loading TM, the reduction peak shifted forward considerably, occurring at 620°C for Co-CrN and at 660°C for Ni-CrN, respectively. The shifted reduction peaks indicate an enhanced reactivity with H_2 owing to the activation effect of TMs. The peaks observed at 226°C and 272°C correspond to the surface reduction of CoO and NiO [65–67]. As depicted in Fig. 3b, N_2 -TG analysis was introduced to study the nitrogen fixation ability of the reduced nitrogen carriers. By comparison, the weight gain of the pristine CrN was 1.3%, whereas the loading of Co, Ni, and Fe increased the value to 7.5%, 5.6%, and 3.2%, respectively. It is hypothesized that TM can also facilitate the nitrogen fixation process of Cr-based nitrogen carriers, thereby forming the basis

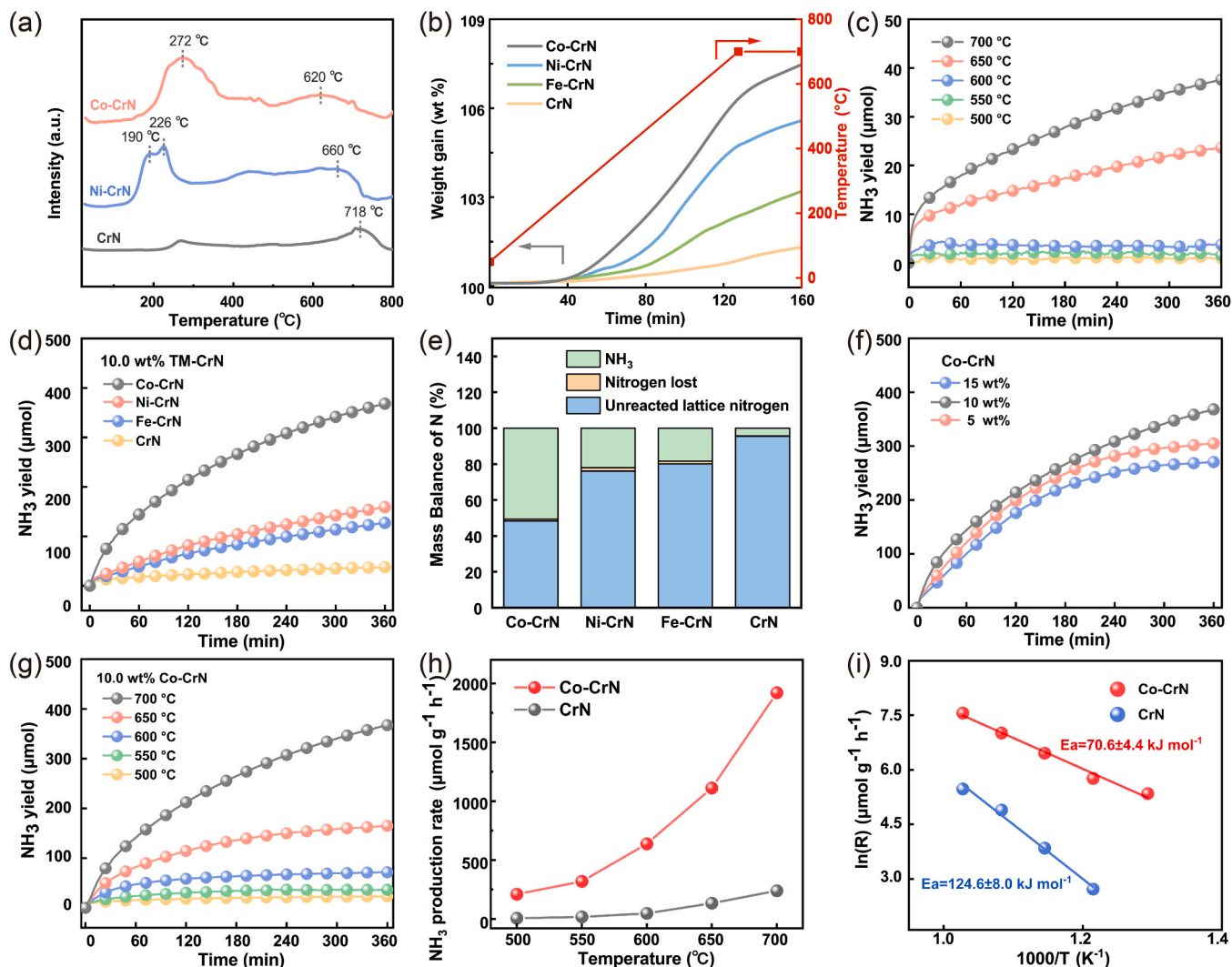


Fig. 3. Nitrogen transfer properties of Cr-based nitrogen carriers. (a) H₂-TPR profiles of selected samples. (b) TG analysis of the pristine CrN and TM-CrN under a flow of N₂ with a ramping rate at 5 °C min⁻¹. (c) NH₃ production amount of the pristine CrN at different temperatures as a function of time (H₂/Ar = 3:1, WHSV = 60,000 ml g⁻¹ h⁻¹). (d) NH₃ production amount of 10 wt% TM-CrN in reacting with H₂ (700 °C, 1 bar). (e) Mass balance of N in the hydrogenation of the pristine CrN and TM-CrN. (f) The influence of Co amount on NH₃ production in Co-CrN (700 °C, 1 bar). (g) NH₃ production amount of 10 wt% Co-CrN at different temperatures as a function of time (H₂/Ar = 3:1, WHSV = 60,000 ml g⁻¹ h⁻¹). (h) The temperature-dependent rate of hydrogenation of CrN and Co-CrN. (i) Corresponding Arrhenius plots of (h).

of realizing CLAS.

To evaluate the reactivity and selectivity of NH₃ production during the hydrogenation stage, systematic investigations were conducted in an H₂/Ar atmosphere. As shown in Fig. 3c, the pristine CrN can only consistently produce NH₃ at temperature higher than 600 °C. An amount of 37.6 μmol NH₃ was generated by the pristine CrN (60 mg), and the average reaction rate of CrN at 700 °C was calculated to be 83.55 μmol g⁻¹ h⁻¹ in the first 6 h. Favorably, the NH₃ yield of TM-loaded CrN shows a tremendous increment (Fig. 3d). Among them, Co-CrN (60 mg) could produce 368.2 μmol NH₃ at 700 °C in the first 6 h, achieving an average NH₃ production rate of 818.2 μmol g⁻¹ h⁻¹. Not only did Co increase the NH₃ production rate by roughly 10 folds, but also it reduced the initial temperature of hydrogenation from 600 °C to 500 °C. However, the instantaneous reaction rate of Cr-based nitrogen carriers decreased with a prolonged reaction time (Fig. S11), possibly due to the consumption of lattice nitrogen. The depletion of lattice nitrogen can also be verified by the diminished peak of CrN in the XRD pattern of the reduced nitrides (Fig. S12). In short, the loading of TMs significantly boosted the directed NH₃ conversion from the lattice nitrogen in CrN.

To further investigate the nitrogen transfer property of Cr-based nitrogen carriers, a nitrogen mass balance analysis was performed and the results were presented in Fig. 3e and Table S3. Attractively, the amount of converted lattice nitrogen was boosted from 4.3% to 50.7% with the promotion of Co. The conversion rate of lattice nitrogen in Ni-CrN and Fe-CrN also achieved 22.3% and 18.4%, respectively. Moreover, the NH₃ generation selectivity of the converted nitrogen was higher than 95% for all samples (98.1% for Co-CrN). It is indicated that only less than 5% of the lattice nitrogen was transformed to N₂ and could not be effectively utilized. As shown in the characterizations of Co-CrN with different Co loading, a moderate level of the decoration is beneficial for nitrogen conversion (Fig. S13). Consequently, the loading of TMs enables lattice nitrogen activation without compromising the high selectivity of NH₃ production.

Owing to the excellent performance of Co-CrN, the NH₃ synthesis property of Co-CrN with different Co loading was further explored (Fig. 3f). They exhibit high levels of reactivity and a similar trend in cumulative NH₃ releasing. However, the NH₃ yield may decrease when Co exceeds a certain threshold, as too much Co decreases the initial nitrogen content of Co-CrN (Table S3). Moreover, the NH₃ production

properties of 10 wt% Co-CrN at different temperatures were investigated (Fig. 3g). In the temperature range of 500–700 °C, the NH_3 yield amount and rate both increased continuously with maximum 15 folds. As shown in Fig. 3h, the ammonia production rate of Co-CrN is much higher than that of the pristine CrN under the same condition. In the hydrogenation with H_2 , the activation energy (E_a) for CrN and Co-CrN were fitted to be 124.6 and 74.6 kJ mol^{-1} accordingly (Fig. 3i), reflecting a significant promotion of lattice nitrogen reactivity with the Co loading.

3.3. CLAS performance of Cr-based nitrogen carriers

The CLAS performances of Cr-based nitrogen carriers were evaluated based on the release/charge of lattice nitrogen. As shown in Fig. 4a, the NH_3 production rate in a CLAS process was dramatically enhanced upon TMs-catalyzed chromium nitride. The loop mediated by Co-CrN produced NH_3 at a rate of 466.1 $\mu\text{mol g}^{-1} \text{h}^{-1}$, which is one order of magnitude higher than that of the pristine CrN under the same condition (700 °C, 1 bar). With the alternation of H_2 and N_2 , a periodic NH_3 signal was clearly observed (Fig. S14). Fig. 4b shows the variation of the average NH_3 production rate as a function of temperature in TM-CrN mediated CLAS. It can be seen that Co-CrN is reliable in completing the looping reaction at a lower temperature (500 °C), and performs a remarkable activity as the temperature rises. Furthermore, the temperature dependent activity of Co-CrN with different Co loading was experimentally identified (Fig. 4c). Co-CrN with 15 wt% and 10 wt% Co

loadings exhibited comparable NH_3 production rates at temperature below 650 °C, while the rate of 15 wt% Co-CrN was further boosted at 700 °C reaching 548.3 $\mu\text{mol g}^{-1} \text{h}^{-1}$. It's worth specifying that no peak of cobalt nitride was detected by XRD in the cycled Co-CrN, indicating that the nitrogen in NH_3 was obtained from CrN.

In addition, Co-CrN exhibited enhanced CLAS performance in comparison with that in thermo-catalytic ammonia synthesis, manifesting the superiority of CLAS using Co-CrN. The thermo-catalytic reactivity of Co-CrN was evaluated by the final ammonia synthesis rate as shown in Fig. S15. The CLAS rate of Co-CrN is around 3–4 folds that of thermo-catalytic ammonia synthesis. These results provide clear evidence that the combination of Co and CrN facilitates the activation of lattice nitrogen and simultaneously enhances the nitrogen fixation in reduced nitrides. Also, the comparison between the NH_3 production rate in CLAS and the thermal-catalytic process illustrates that TM-CrN with dual active sites may circumvent the competitive adsorption of intermediate species in NH_3 synthesis (Fig. S15). On this basis, the long-term stability of 10 wt% Co-CrN in CLAS was evaluated (Fig. 4d). The NH_3 production rate decreased from an initial rate of approximately 500 $\mu\text{mol g}^{-1} \text{h}^{-1}$ to 430 $\mu\text{mol g}^{-1} \text{h}^{-1}$ and stabilized at that level in the subsequent 10 consecutive cycles. Table S4 shows the performance of other reported TMNx for nitrogen transfer property and cyclability. The splendid reactivity of Cr-based nitrogen carriers proceeds the scope of their utilization as nitrogen activation centers.

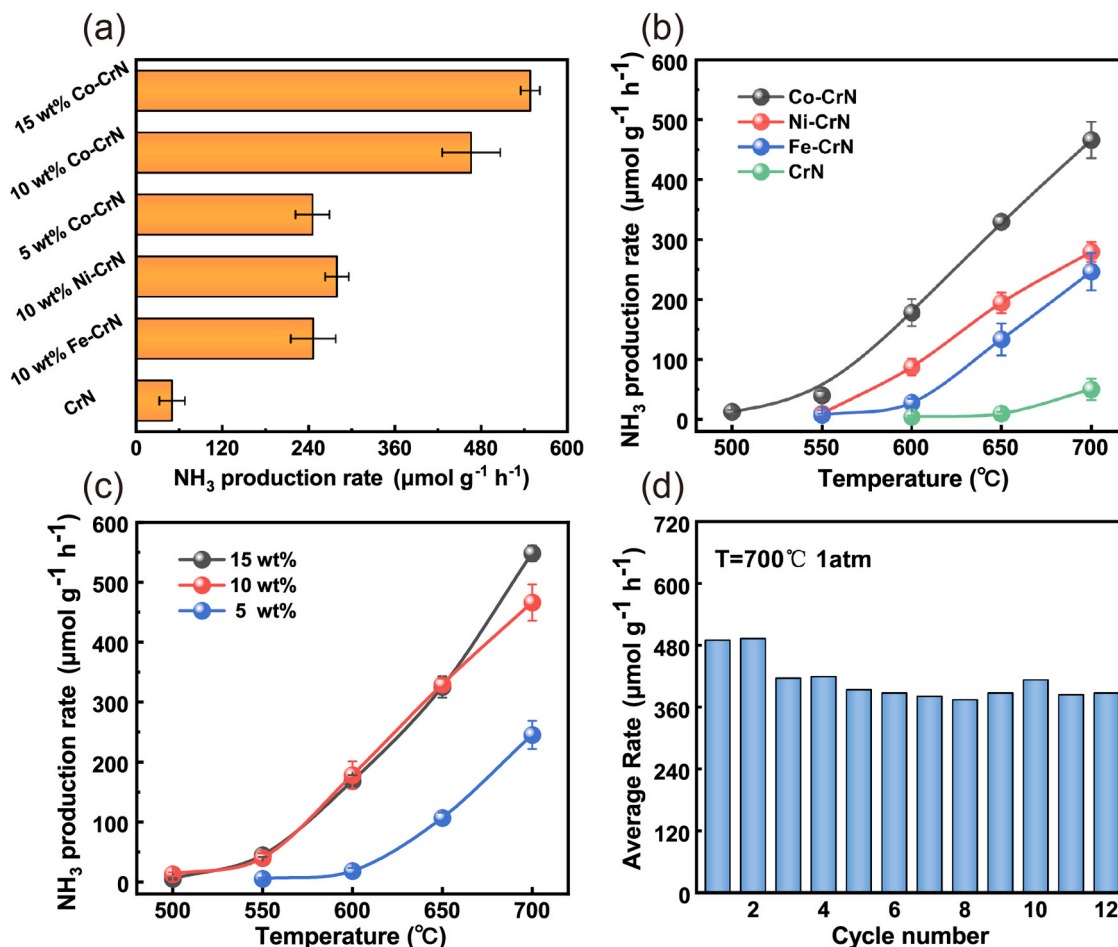


Fig. 4. CLAS performance of Cr-based nitrogen carriers. (a) The average NH_3 production rate of the pristine CrN and TM-CrN under an alternative flow of N_2 and H_2 (700 °C, WHSV = 60,000 $\text{ml g}^{-1} \text{h}^{-1}$). (b) The average NH_3 synthesis rate of TM-CrN as a function of temperature in CLAS. (c) The temperature dependent activity of Co-CrN with different Co loading. Error bars denote the standard deviation of the recorded rates in at least three separated tests. (d) Cyclic CLAS performance of 10 wt% Co-CrN at 700 °C, 1 bar.

3.4. Theoretical insight

Density functional theory (DFT) calculations were performed to identify the atomic migration and the synergistic mechanism on Co-CrN surface. An all-atom model of Co-CrN(001) with abundant active sites was built under the guidance of characterization results (Fig. S16) [68, 69]. It's notable that the (001) surface was cleaved in the same configuration as (200) since the CrN features a face-centered cubic structure [32]. Moreover, the Co₈ cluster with the structure described in Fig. S17 was found to possess lower formation energy [70]. Therefore, the computation model of a Co₈ cluster loaded CrN(001) surface was optimized for further insights. The adsorption energies and geometries of intermediate species on Co-CrN are illustrated in Table S5 and Fig. S18. It is found that H atoms are favorably adsorbed on the hcc site of the Co₈ cluster, while the active nitrogen is present as lattice nitrogen. The diffused H* tends to bind lattice nitrogen to form NH*, and the bond length of Cr–N is stretched from 2.26 Å to 2.74 Å. The most stable adsorption site for NH₂* is the bridge of the Cr atom, with strong adsorption energy of $E_{\text{ads}} = -3.84$ eV, which is higher than those of other reported TMNx [36]. NH₃* tends to adsorb on the top of a single Cr atom with a N–Cr bond length of 2.13 Å and outwards stretching of the hydrogen atom. The N–H bond length and H–N–H cone angle in NH₃* are close to those of the relaxed NH₃ molecules.

The free energy and structural evolution along the predicted pathway of Co-CrN for CLAS are described in Fig. 5. The overall process is decoupled into two stages: the hydrogenation of lattice nitrogen and the nitridation occurring on V_N, which is consistent with the famous Mars–van Krevelen mechanism [71]. The starting state (step I in Fig. 5) is perfect Co₈-Cr₃₂N₃₂. H₂ dissociation occurs continuously on the Co₈ cluster (I → II) with a negligible dissociation energy barrier (lower than 0.03 eV) [72]. However, on the CrN substrate devoid Co cluster, the adsorption of H₂ is difficult with an adsorption energy of plus 0.28 eV. This indicates that the modulation effect of Co is realized by increasing the coverage of dissociated H* on Co-CrN surface (Fig. S19). Subsequently, the diffused H* tends to attack the lattice nitrogen to generate NH_x (x = 1–3) species, which may finally form an NH₃ molecule (II → VI). The desorption energy (VI → VII) of NH₃ is only 0.26 eV, manifesting the high NH₃ production selectivity on the surface of Co-CrN (001). From the starting state to the generation of the first NH₃ molecule, the free energy of the system elevates slightly due to the formation of nitrogen vacancy (V_N). Thereafter, the adjacent lattice nitrogen is attacked by H* until forming the second NH₃ molecule and a new V_N (VII → XII). The regeneration process on the surface is accomplished by the adsorptive dissociation of N₂ at V_N, which is compensated by the dissociated N (XII → XIV). The free energy of the entire CLAS process decreases by approximately –1.21 eV from N₂ to NH₃, in consistent with the exothermic process of NH₃ generation [73].

The magnitude of the transition-state energy barrier for the elementary reactions in CLAS was further investigated by using a climbing image (CI-NEB) method and the results are presented in Fig. S20 and Table S6. As illustrated in the table, the energy barrier associated with N₂ activation at V_N is only 1.24 eV, which is obviously lower than that in all hydrogenation steps. Fig. S21 depicts the stretching of N≡N on the dual V_N of CrN and Co₈-CrN. When the surface contains a Co₈ cluster, the bond length in N₂ is further extended from 1.308 Å (only CrN) to 1.353 Å (1.12 Å in vacuum). The energy barrier of N₂ adsorption dissociation on CrN is calculated 1.31 eV, higher than that on Co₈-CrN. These results demonstrate the remarkable nitrogen fixation ability of Co-CrN under the promotion of V_N. Moreover, the highest energy barrier (1.63 eV) is present in the conversion of NH₂* to NH₃*, which matches the strong adsorption of NH₂* as mentioned above. This indicates that the rate-determining step for CLAS is associated with the combination of H* and N_{lattice}. The proposed reaction mechanism in this work involves N₂ activation on V_N and modulation of H* with another metal, thus achieving a successful reduction of the energy barrier. In consequence, the well-known “scaling relationship” could be avoided

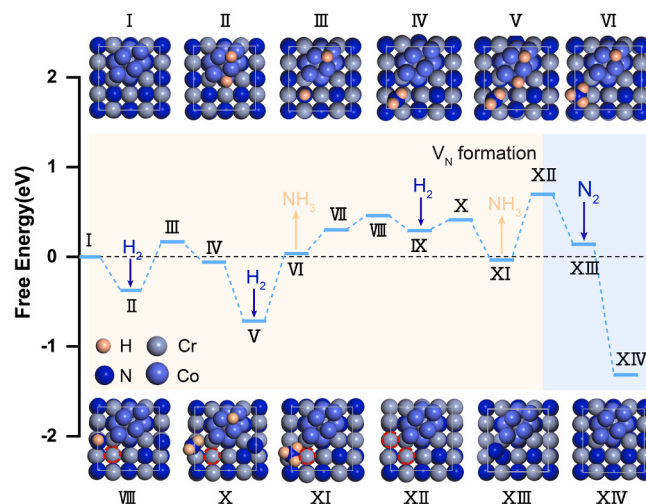


Fig. 5. DFT studies of the reaction pathway of Co-CrN for CLAS. The proposed hydrogenation and N₂ activation mechanism for CLAS on the Co-CrN(001) surface is shown. The central plot displays the calculated free energy diagram, and the structures of the selected intermediates in corresponding steps (I → XIV) are shown in the surface model.

via a synergistic interaction between Co₈ clusters and the CrN substrates.

4. Conclusion

In conclusion, a promising and efficient Cr-based nitrogen carrier for CLAS under ambient pressure is designed and demonstrated in this work. As a nitrogen transfer reagent, TM-loaded CrN performs well-controlled reactivity by converting maximum 50.7% of the lattice nitrogen and maintains excellent NH₃ conversion selectivity at 98.1%. The chemical loop mediated by Co-CrN produces NH₃ at a rate of as high as 466.1 μmol g^{−1} h^{−1} in more than 12 cycles under atmospheric pressure, one order of magnitude higher than that of the pristine CrN, demonstrating a remarkable enhancement in N₂ activation. The proposed reaction path of CLAS on Co-CrN is identified through DFT insight, revealing the nitrogen vacancy regeneration mechanism and the synergistic interaction between Co clusters and CrN substrate. This study explores the potential for decentralized and sustainable ammonia synthesis based on chemical looping approach with optimized composite nitrogen carriers.

CRedit authorship contribution statement

Sijun Wang, Feng Gong: Conceptualization, Methodology, Investigation, Validation, Formal analysis, Writing – original draft, Writing – review & editing. **Feng Gong, Rui Xiao:** Project administration, Resources, Writing – review & editing, Supervision. **Qiang Zhou, Yunlong Xie:** Methodology, Validation, Formal analysis. **Hao Li, Menglin Li:** Writing – review & editing, Formal analysis. **Enkang Fu, Peng Yang, Yuhang Jing:** Investigation, Validation.

Declaration of Competing Interest

The authors declare that they have no known competing financial interests or personal relationships that could have appeared to influence the work reported in this paper.

Data availability

Data will be made available on request.

Acknowledgement

The authors would like to thank the financial support from the National Natural Science Foundation of China (52076045) and the Ministry of Science and Technology of China (2022YFB4201802, 2019YFC1906700). Y.L. Xie was supported by the Natural Science Foundation of Hubei Province (No. 2021CFB574). This research work is supported by the Big Data Computing Center of Southeast University.

Appendix A. Supporting information

Supplementary data associated with this article can be found in the online version at doi:10.1016/j.apcatb.2023.123134.

References

- [1] A. Valera-Medina, H. Xiao, M. Owen-Jones, W.I.F. David, P.J. Bowen, Ammonia for power, *Prog. Energy Combust. Sci.* 69 (2018) 63–102.
- [2] V. Smil, Detonator of the population explosion, *Nature* 400 (1999), 415–415.
- [3] A. Klerke, C.H. Christensen, J.K. Norskov, T. Vegge, Ammonia for hydrogen storage: challenges and opportunities, *J. Mater. Chem.* 18 (2008) 2304–2310.
- [4] J.W. Makepeace, T. He, C. Weidenthaler, T.R. Jensen, F. Chang, T. Vegge, P. Ngene, Y. Kojima, P.E. de Jongh, P. Chen, W.I.F. David, Reversible ammonia-based and liquid organic hydrogen carriers for high-density hydrogen storage: recent progress, *Int. J. Hydrog. Energy* 44 (2019) 7746–7767.
- [5] J.W. Erisman, M.A. Sutton, J. Galloway, Z. Klimont, W. Winiwarter, How a century of ammonia synthesis changed the world, *Nat. Geosci.* 1 (2008) 636–639.
- [6] L. Wang, M.K. Xia, H. Wang, K.F. Huang, C.X. Qian, C.T. Maravelias, G.A. Ozin, Greening ammonia toward the solar ammonia refinery, *Joule* 2 (2018) 1055–1074.
- [7] W. Gao, J. Guo, P. Wang, Q. Wang, F. Chang, Q. Pei, W. Zhang, L. Liu, P. Chen, Production of ammonia via a chemical looping process based on metal imides as nitrogen carriers, *Nat. Energy* 3 (2018) 1067–1075.
- [8] J.N. Galloway, A.R. Townsend, J.W. Erisman, M. Bekunda, Z. Cai, J.R. Freney, L. A. Martinelli, S.P. Seitzinger, M.A. Sutton, Transformation of the nitrogen cycle: recent trends, questions, and potential solutions, *Science* 320 (2008) 889–892.
- [9] Q.R. Wang, J.P. Guo, P. Chen, Recent progress towards mild-condition ammonia synthesis, *J. Energy Chem.* 36 (2019) 25–36.
- [10] F. Chang, W.B. Gao, J.P. Guo, P. Chen, Emerging materials and methods toward ammonia-based energy storage and conversion, *Adv. Mater.* 33 (2021).
- [11] Q. Lai, T. Cai, S.C.E. Tsang, X. Chen, R. Ye, Z. Xu, M.D. Argyle, D. Ding, Y. Chen, J. Wang, A.G. Russell, Y. Wu, J. Liu, M. Fan, Chemical looping based ammonia production-A promising pathway for production of the noncarbon fuel, *Sci. Bull.* 67 (2022) 2124–2138.
- [12] J.K. Norskov, J.G. Chen, R. Miranda, T. Fitzsimmons, R.G. Stack, Sustainable ammonia synthesis – exploring the scientific challenges associated with discovering alternative, *Sustain. Process. Ammon. Prod.* (2016).
- [13] R. Michalsky, A.M. Avram, B.A. Peterson, P.H. Pfromm, A.A. Peterson, Chemical looping of metal nitride catalysts: low-pressure ammonia synthesis for energy storage, *Chem. Sci.* 6 (2015) 3965–3974.
- [14] F. Haber, G.V. Oordt, Über die bildung von ammoniak den elementen, *Z. für Anorg. und Allg. Chem.* 44 (1905) 341–378.
- [15] A.R. Frank, On the utilisation of the atmospheric nitrogen in the production of calcium cyanamide, and its use in agriculture and chemistry, *Trans. Faraday Soc.* 4 (1908) 99–114.
- [16] A.M. Alexander, J.S.J. Hargreaves, C. Mitchell, The reduction of various nitrides under hydrogen: Ni_3N , Cu_3N , Zn_3N_2 and Ta_3N_5 , *Top. Catal.* 55 (2012) 1046–1053.
- [17] S. Laassiri, C.D. Zeinalipour-Yazdi, C.R.A. Catlow, J.S.J. Hargreaves, Nitrogen transfer properties in tantalum nitride based material, *Catal. Today* 286 (2017) 147–155.
- [18] A.M. Alexander, J.S.J. Hargreaves, C. Mitchell, The denitridation of nitrides of iron, cobalt and rhenium under hydrogen, *Top. Catal.* 56 (2013) 1963–1969.
- [19] S. Yang, T. Zhang, Y. Yang, B. Wang, J. Li, Z. Gong, Z. Yao, W. Du, S. Liu, Z. Yu, Molybdenum-based nitrogen carrier for ammonia production via a chemical looping route, *Appl. Catal. B Environ.* 312 (2022), 121404.
- [20] S. Laassiri, C.D. Zeinalipour-Yazdi, C.R.A. Catlow, J.S.J. Hargreaves, The potential of manganese nitride based materials as nitrogen transfer reagents for nitrogen chemical looping, *Appl. Catal. B Environ.* 223 (2018) 60–66.
- [21] B.Y. Wang, H.J. Guo, X.L. Yin, L.H. Shen, N-sorption capability of Al_2O_3 -supported Mn-/Fe-based nitrogen carriers during chemical looping ammonia synthesis technology, *Fuels* 34 (2020) 10247–10255.
- [22] B. Wang, X. Yin, P. Wang, L. Shen, Chemical looping ammonia synthesis at atmospheric pressure benefiting from synergistic effect of Mn- and Fe-based nitrogen carriers, *Int. J. Hydrog. Energy* 48 (2022) 2705–2717.
- [23] J.L. Hua, K. Wang, Q. Wang, R.J. Peng, Feasibility of Fe-based nitrogen carrier for chemical looping ammonia synthesis: thermodynamics, *J. Therm. Anal. Calorim.* 146 (2021) 673–680.
- [24] D. McKay, D.H. Gregory, J.S.J. Hargreaves, S.M. Hunter, X.L. Sun, Towards nitrogen transfer catalysis: reactive lattice nitrogen in cobalt molybdenum nitride, *Chem. Commun.* (2007) 3051–3053.
- [25] D.H. Gregory, J.S.J. Hargreaves, S.M. Hunter, On the regeneration of $\text{Co}_3\text{Mo}_3\text{N}$ from $\text{Co}_6\text{Mo}_6\text{N}$ with N_2 , *Catal. Lett.* 141 (2011) 22–26.
- [26] S.M. Hunter, D.H. Gregory, J.S.J. Hargreaves, M. Richard, D. Duprez, N. Bion, A study of N-15/N-14 isotopic exchange over cobalt molybdenum nitrides, *ACS Catal.* 3 (2013) 1719–1725.
- [27] J.S.J. Hargreaves, Nitrides as ammonia synthesis catalysts and as potential nitrogen transfer reagents, *Appl. Petrochem. Res.* 4 (2014) 3–10.
- [28] C.D. Zeinalipour-Yazdi, J.S.J. Hargreaves, S. Laassiri, C.R.A. Catlow, The integration of experiment and computational modelling in heterogeneously catalysed ammonia synthesis over metal nitrides, *Phys. Chem. Chem. Phys.* 20 (2018) 21803–21808.
- [29] C.D. Zeinalipour-Yazdi, J.S.J. Hargreaves, C.R.A. Catlow, Nitrogen activation in a Mars–van Krevelen mechanism for ammonia synthesis on $\text{Co}_3\text{Mo}_3\text{N}$, *J. Phys. Chem. C* 119 (2015) 28368–28376.
- [30] A. Daisley, J.S.J. Hargreaves, Metal nitrides, the Mars–van Krevelen mechanism and heterogeneously catalysed ammonia synthesis, *Catal. Today* (2022), 113874.
- [31] A.J. Medford, A. Vojvodic, J.S. Hummelshøj, J. Voss, F. Abild-Pedersen, F. Studt, T. Bligaard, A. Nilsson, J.K. Norskov, From the Sabatier principle to a predictive theory of transition-metal heterogeneous catalysis, *J. Catal.* 328 (2015) 36–42.
- [32] T.N. Ye, S.W. Park, Y.F. Lu, J. Li, M. Sasase, M. Kitano, T. Tada, H. Hosono, Vacancy-enabled N(2) activation for ammonia synthesis on an Ni-loaded catalyst, *Nature* 583 (2020) 391–395.
- [33] T.N. Ye, S.W. Park, Y.F. Lu, J. Li, M. Sasase, M. Kitano, H. Hosono, Contribution of nitrogen vacancies to ammonia synthesis over metal nitride catalysts, *J. Am. Chem. Soc.* 142 (2020) 14374–14383.
- [34] Y.F. Lu, T.N. Ye, J. Li, Z.C. Li, H.T. Guan, M. Sasase, Y. Niwa, H. Abe, Q. Li, F. S. Pan, M. Kitano, H. Hosono, Approach to chemically durable nickel and cobalt lanthanum-nitride-based catalysts for ammonia synthesis, *Angew. Chem. Int. Ed.* 61 (2022).
- [35] H.X. Yan, W.B. Gao, Q.R. Wang, Y.Q. Guan, S. Feng, H. Wu, Q. Guo, H.J. Cao, J. P. Guo, P. Chen, Lithium palladium hydride promotes chemical looping ammonia synthesis mediated by lithium imide and hydride, *J. Phys. Chem. C* 125 (2021) 6716–6722.
- [36] N. Shan, V. Chikan, P. Pfromm, B. Liu, Fe and Ni dopants facilitating ammonia synthesis on Mn_4N and mechanistic insights from first-principles methods, *J. Phys. Chem. C* 122 (2018) 6109–6116.
- [37] N.N. Shan, C.R. Huang, R.T. Lee, N. Manavi, L.B. Xu, V. Chikan, P.H. Pfromm, B. Liu, Manipulating the geometric and electronic structures of manganese nitrides for ammonia synthesis, *ChemCatChem* 12 (2020) 2233–2244.
- [38] Y. Goto, A. Daisley, J.S.J. Hargreaves, Towards anti-perovskite nitrides as potential nitrogen storage materials for chemical looping ammonia production: reduction of Co_3ZnN , Ni_3ZnN , Co_3InN and Ni_3InN under hydrogen, *Catal. Today* 364 (2021) 196–201.
- [39] Y. Qiu, L. Gao, Synthesis of nanocrystalline CrN from $\text{Cr}[\text{OC}(\text{NH}_2)_2]_6\text{Cl}_3$ coordination compound, *Mater. Res. Bull.* 38 (2003) 1551–1557.
- [40] B. Das, M.V. Reddy, G.V.S. Rao, B.V.R. Chowdari, Synthesis and Li-storage behavior of CrN nanoparticles, *RSC Adv.* 2 (2012) 9022–9028.
- [41] J. Ren, Q.Z. Jiao, T. Wang, Y.F. Geng, H.S. Li, Q. Wu, D.X. Shi, Y. Zhao, C.H. Feng, $\text{CoMoS}_4/\text{CeO}_2$ -gamma- Al_2O_3 catalyst: preparation and performance in catalytic reduction of SO_2 , *Chin. J. Inorg. Chem.* 37 (2021) 844–852.
- [42] E. Fu, Y. Qiu, H. Lu, S. Wang, L. Liu, H. Feng, Y. Yang, Z. Wu, Y. Xie, F. Gong, R. Xiao, Enhanced NH_3 decomposition for H_2 production over bimetallic $\text{M}(\text{M}=\text{Co}, \text{Fe}, \text{Cu})/\text{Ni}/\text{Al}_2\text{O}_3$, *Fuel Process. Technol.* 221 (2021), 106945.
- [43] W.H. Guo, Z.B. Liang, Y.Q. Tang, K.T. Cai, T.J. Qiu, Y.X. Wu, K.X. Zhang, S. Gao, R. Q. Zou, Understanding the lattice nitrogen stability and deactivation pathways of cubic CrN nanoparticles in the electrochemical nitrogen reduction reaction, *J. Mater. Chem. A* 9 (2021) 8568–8575.
- [44] G. Vazquez, E. Alvarez, J.M. Navaza, Surface tension of alcohol + water from 20 to 50 °C, *J. Chem. Eng. Data* 40 (1995) 611–614.
- [45] X.G. Kong, F.B. Surani, Y. Qiao, Effects of addition of ethanol on the infiltration pressure of a mesoporous silica, *J. Mater. Res.* 20 (2005) 1042–1045.
- [46] A. Daisley, J.S.J. Hargreaves, The role of interstitial species upon the ammonia synthesis activity of ternary Fe–Mo–C(N) and Ni–Mo–C(N) phases, *J. Energy Chem.* 39 (2019) 170–175.
- [47] G. Kresse, J. Furthmüller, Efficient iterative schemes for ab initio total-energy calculations using a plane-wave basis set, *Phys. Rev. B* 54 (1996) 11169–11186.
- [48] G. Kresse, D. Joubert, From ultrasoft pseudopotentials to the projector augmented-wave method, *Phys. Rev. B* 59 (1999) 1758–1775.
- [49] Q. Zhou, F. Gong, Y. Xie, D. Xia, Z. Hu, S. Wang, L. Liu, R. Xiao, A general strategy for designing metal-free catalysts for highly-efficient nitric oxide reduction to ammonia, *Fuel* 310 (2022), 122442.
- [50] R.V. de Amorim, K.E.A. Batista, G.R. Nagurniak, R.P. Orenha, R.L.T. Parreira, M. J. Piotrowski, CO, NO, and SO adsorption on Ni nanoclusters: a DFT investigation, *Dalton Trans.* 49 (2020) 6407–6417.
- [51] J.R. Zhang, Y.Q. Zhao, L. Chen, S.F. Yin, M.Q. Cai, Density functional theory calculation on facet-dependent photocatalytic activity of MoS_2/CdS heterostructures, *Appl. Surf. Sci.* 469 (2019) 27–33.
- [52] Y.L. Wang, Y. Tian, Z.L. Lang, W. Guan, L.K. Yan, A highly efficient Z-scheme B-doped g- $\text{C}_3\text{N}_4/\text{SnS}_2$ photocatalyst for CO_2 reduction reaction: a computational study, *J. Mater. Chem. A* 6 (2018) 21056–21063.
- [53] Z.Y. Luo, Y.X. Ouyang, H. Zhang, M.L. Xiao, J.J. Ge, Z. Jiang, J.L. Wang, D. M. Tang, X.Z. Cao, C.P. Liu, W. Xing, Chemically activating MoS_2 via spontaneous atomic palladium interfacial doping towards efficient hydrogen evolution, *Nat. Commun.* 9 (2018) 2120.
- [54] G. Henkelman, H. Jonsson, Improved tangent estimate in the nudged elastic band method for finding minimum energy paths and saddle points, *J. Chem. Phys.* 113 (2000) 9978–9985.

- [55] Y. Abghoui, E. Skúlason, Computational predictions of catalytic activity of zincblende (110) surfaces of metal nitrides for electrochemical ammonia synthesis, *J. Phys. Chem. C* 121 (2017) 6141–6151.
- [56] T.W. Ouyang, W.Y. Fan, J.Q. Guo, Y.N. Zheng, X.H. Yin, Y.L. Shen, DFT study on Ag loaded 2H-MoS₂ for understanding the mechanism of improved photocatalytic reduction of CO₂, *Phys. Chem. Chem. Phys.* 22 (2020) 10305–10313.
- [57] Q. Zhou, F. Gong, Y. Xie, R. Xiao, 1+1>2: learning from the interfacial modulation on single-atom electrocatalysts to design dual-atom electrocatalysts for dinitrogen reduction, *Green. Energy Environ.* (2022), <https://doi.org/10.1016/j.gee.2022.06.005>.
- [58] A. Yamaguchi, R.B. Penland, S. Mizushima, T.J. Lane, C. Curran, J.V. Quagliano, Infrared absorption spectra of inorganic coordination complexes. XIV. Infrared studies of some metal thiourea complexes 1a, *J. Am. Chem. Soc.* 80 (1958) 527–529.
- [59] I. Milošev, H.H. Strehblow, B. Navinšek, M. Metikoš-Huković, Electrochemical and thermal oxidation of TiN coatings studied by XPS, *Surf. Interface Anal.* 23 (1995) 529–539.
- [60] F. Esaka, K. Furuya, H. Shimada, M. Imamura, N. Matsubayashi, T. Sato, A. Nishijima, T. Kikuchi, A. Kawana, H. Ichimura, Depth profiling of surface oxidized TiAlN film by synchrotron radiation excited X-ray photoelectron spectroscopy, *Surf. Sci.* 377–379 (1997) 197–200.
- [61] Y. Yuan, J.H. Wang, S. Adimi, H.J. Shen, T. Thomas, R.G. Ma, J.P. Attfield, M. H. Yang, Zirconium nitride catalysts surpass platinum for oxygen reduction, *Nat. Mater.* 19 (2020) 282–286.
- [62] J. Wang, Q. Zhong, Y. Xiong, D. Cheng, Y. Zeng, Y. Bu, Fabrication of 3D Co-doped Ni-based MOF hierarchical micro-flowers as a high-performance electrode material for supercapacitors, *Appl. Surf. Sci.* 483 (2019) 1158–1165.
- [63] X.J. Meng, W.L. Qi, W.D. Kuang, S. Adimi, H.C. Guo, T. Thomas, S.Q. Liu, Z. P. Wang, M.H. Yang, Chromium-titanium nitride as an efficient co-catalyst for photocatalytic hydrogen production, *J. Mater. Chem. A* 8 (2020) 15774–15781.
- [64] I. Milošev, H.H. Strehblow, M. Gabersček, B.J.S. Navinšek, Electrochemical oxidation of Zn hard (PVD) coatings studied by XPS, *Surf. Interface Anal.* 24 (1996) 448–458.
- [65] J.A. Rodriguez, J.Y. Kim, J.C. Hanson, M. Pérez, A.I. Frenkel, Reduction of CuO in H₂: in situ time-resolved XRD studies, *Catal. Lett.* 85 (2003) 247–254.
- [66] J.A. Rodriguez, J.C. Hanson, A.I. Frenkel, J.Y. Kim, M. Pérez, Experimental and theoretical studies on the reaction of H₂ with NiO: role of O vacancies and mechanism for oxide reduction, *J. Am. Chem. Soc.* 124 (2002) 346–354.
- [67] A.K. Galwey, B.V. L'vov, The mechanism and kinetics of NiO reduction by hydrogen, *J. Therm. Anal. Calorim.* 110 (2012) 601–610.
- [68] Y.Q. Guan, C.W. Liu, Q.R. Wang, W.B. Gao, H.A. Hansen, J.P. Guo, T. Vegge, P. Chen, Transition-metal-free barium hydride mediates dinitrogen fixation and ammonia synthesis, *Angew. Chem. Int. Ed.* 61 (2022), e202205805.
- [69] K. Honkala, A. Hellman, I.N. Remediakis, A. Logadottir, A. Carlsson, S. Dahl, C. H. Christensen, J.K. Nørskov, Ammonia synthesis from first-principles calculations, *Science* 307 (2005) 555–558.
- [70] A.S. Chaves, M.J. Piotrowski, J.L.F. Da Silva, Evolution of the structural, energetic, and electronic properties of the 3d, 4d, and 5d transition-metal clusters (30 TM_n systems for n=2–15): a density functional theory investigation, *Phys. Chem. Phys.* 19 (2017) 15484–15502.
- [71] Y. Abghoui, E. Skúlason, Electrochemical synthesis of ammonia via Mars-van Krevelen mechanism on the (111) facets of group III–VII transition metal mononitrides, *Catal. Today* 286 (2017) 78–84.
- [72] M. Yu, L. Liu, Q. Wang, L. Jia, B. Hou, Y. Si, D. Li, Y. Zhao, High coverage H₂ adsorption and dissociation on fcc Co surfaces from DFT and thermodynamics, *Int. J. Hydrog. Energy* 43 (2018) 5576–5590.
- [73] A. Hellman, K. Honkala, I.N. Remediakis, Á. Logadóttir, A. Carlsson, S. Dahl, C. H. Christensen, J.K. Nørskov, Insights into ammonia synthesis from first-principles, *Surf. Sci.* 600 (2006) 4264–4268.